

A Monte Carlo study of the chiral columnar organizations of dissymmetric discotic mesogens

R. Berardi, M. Cecchini,^{a)} and C. Zannoni

Dipartimento di Chimica Fisica e Inorganica and INSTM, Università, Viale Risorgimento 4, 40136 Bologna, Italy

(Received 10 April 2003; accepted 15 August 2003)

We study the relation between the chirality of a discotic mesogen and that of the chiral columnar aggregates that they can spontaneously form by self-assembly. We discuss first the different types of chiral columns that can be in principle obtained. We introduce then a simple two-site Gay–Berne dissymmetric molecular model where chirality can be easily varied and perform extensive NPT Monte Carlo simulations of samples of these particles for different chiralities. At low temperatures we find nematic discotic and columnar mesophases formed by overall chiral columns and we analyze the results in terms of suitably defined observables and chiral correlation functions. We find that, at least for our model system, the columnar chirality is not originating from a regular helical or spiral arrangement of particles but it is mainly due to one-particle high-chirality defects separated by low-chirality domains. © 2003 American Institute of Physics. [DOI: 10.1063/1.1616913]

I. INTRODUCTION

Chirality is a far reaching property in the large scale supermolecular organization of living matter and materials.^{1–6} Particularly striking is the formation of twisted nematic (cholesteric), and columnar liquid crystal phases, where minute chiral perturbations at molecular level produce macroscopically detectable effects. Indeed it has been shown long ago by Gray *et al.*⁷ that even an isotopic substitution of a hydrogen with a deuterium, that causes a carbon atom of a mesogen to become dissymmetric, is sufficient to deform a nematic into a twisted, N^* structure. These effects and more generally chiral versions of liquid crystalline phases are known both for rodlike molecules and their calamitic (nematic, smectic C) type phases as well as for discotic mesogens and their nematic and columnar phases. Of these two classes, calamitic phases are by far the most studied, if only because chiral discotics have been discovered and characterized rather recently.⁸ Chiral columnar mesophases are however particularly interesting,⁹ also because of their ferroelectric¹⁰ properties, and a number of these chiral columnar systems have now been prepared and their properties studied.^{11–16} From the theory and modelling point of view the relation between a discotic and its chirality and the mesophases formed is certainly not clear. This is partly due to the complexity of the molecular structures that can give chiral columns and the difficulty in identifying a precise relation between some key molecular features and observable properties. In this paper we have thus chosen a very simple model for a chiral discotic molecule, formed by two suitably oriented interpenetrating Gay–Berne¹⁷ squashed ellipsoids. We shall see later on that varying the size of the second disk with respect to the first one, molecular chirality can be varied in a controlled way. The model is reminiscent of molecules with planar chirality¹² where handedness results from the arrangement of out of plane groups with respect to the ref-

erence plane, rather than by introduction of chiral carbons. We then consider some of the main types of chiral columnar organizations that can be generated and discuss how to classify and distinguish them by using suitably introduced observables. For instance, chiral columns can have collinear centres along the column axis, with tilt and twist propagating along the column or alternatively they can also have molecular centers describing a spatial helix around the column axis. We have then quantified this in terms of a set of chiral correlations and other observables that can, in principle, be obtained from computer simulations. This should help in establishing how to actually detect from simulation results what organization is obtained. With these tools available, we perform a set of Monte Carlo (MC) (Refs. 18–20) computer simulations on three types of disks with different chirality and, applying the techniques just mentioned, we discuss the organizations obtained. It is worth noting that chirality effects on one hand and the difference between the different chiral structures on the other are rather small and that it is not at all obvious that computer simulations can give the desired information particularly in the presence of numerical errors and defects. Testing this point will also be one aim of this work.

II. MOLECULAR MODELLING

A large number of chiral discotic mesogens can be represented as “decorated disks” where a suitable set of substituents attached to a planar core renders the whole molecule chiral. One of the simplest models of these discotic mesogens is a chiral two-sites (CTS) one where the central core unit is represented by a single oblate ellipsoid with uniaxial or biaxial symmetry and the peripheral residues, responsible of the overall molecular chirality, by the insertion of a second, typically smaller, transversal disk (see Fig. 1). Clearly in this schematization, the first site represents the reference planar structure of the mesogen (“core”) typically formed by aromatic condensed rings and possibly other rigidly connected groups. The central site can therefore be

^{a)}Present address: Department of Biochemistry, University of Zürich, Winterthurerstraße 190, CH-8057 Zürich, Switzerland.

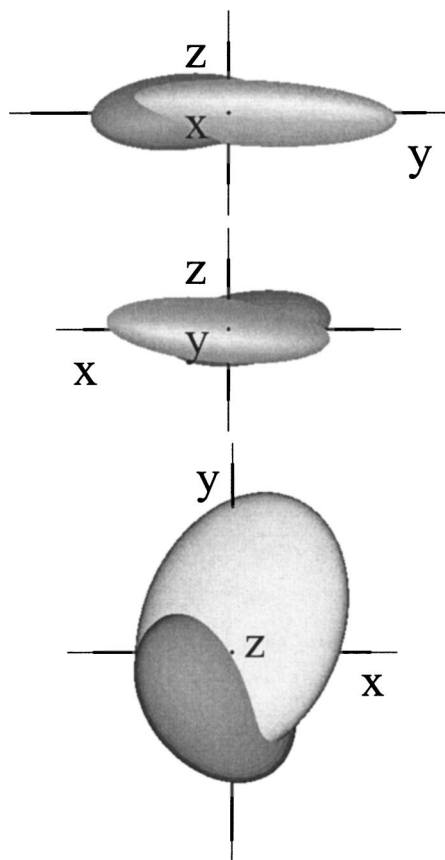


FIG. 1. Modelization of a chiral CTS discotic molecule with two biaxial Gay-Berne particles (from top to bottom mol-X, mol-Y, and mol-Z axes views). The molecular frame, centered on the center of mass and oriented with respect to the moment of inertia is also shown. GB site sizes and relative positions are those of model [c] described in the text.

thought of as having the role of allowing the formation of a columnar liquid crystal phase while the transversal site induces chirality in the mesophase structure itself. We have considered a system formed by a set of N identical CTS particles and to describe the interactions between the ellipsoidal sites belonging to different interacting particles, we have chosen the biaxial heterogeneous version of the Gay-Berne (GB) potential.^{21,22} The GB model itself has proved very successful in generating a variety of liquid crystal phases starting from simple monosite particles,^{23,24} and, in particular, GB disks originate N_D and columnar phases.

The potential between a pair of multisite molecules i and j is written as

$$U_{ij}(\omega_i, \omega_j, \mathbf{r}_{ij}) = \sum_{a \in i, b \in j} U_{ab}^{\text{GBX}}(\omega_a, \omega_b, \mathbf{r}_{ab}), \quad (1)$$

where the site-site interaction is

$$U_{ab}^{\text{GBX}}(\omega_a, \omega_b, \mathbf{r}_{ab}) = 4\epsilon_0 \epsilon(\omega_a, \omega_b, \hat{\mathbf{r}}_{ab}) \times \left[\left(\frac{\sigma_c}{r_{ab} - \sigma(\omega_a, \omega_b, \hat{\mathbf{r}}_{ab}) + \sigma_c} \right)^{12} - \left(\frac{\sigma_c}{r_{ab} - \sigma(\omega_a, \omega_b, \hat{\mathbf{r}}_{ab}) + \sigma_c} \right)^6 \right]. \quad (2)$$

The biaxial ellipsoids representing the sites have orientation ω_a , and ω_b (we use Rose²⁵ notation for rotations) and their site-site interparticle vector is $\mathbf{r}_{ab} = \mathbf{r}_b - \mathbf{r}_a = r_{ab} \hat{\mathbf{r}}_{ab}$ with length r_{ab} , where we use the cap to indicate a unit vector. Since the molecules are rigid there is a simple geometrical relation between the molecular orientations ω_i , and ω_j , the center-center intermolecular vector $\mathbf{r}_{ij} = \mathbf{r}_j - \mathbf{r}_i = r_{ij} \hat{\mathbf{r}}_{ij}$ and the sites orientations and positions. The potential contains an anisotropic contact distance, $\sigma(\omega_a, \omega_b, \hat{\mathbf{r}}_{ab})$, and an interaction term, $\epsilon(\omega_a, \omega_b, \hat{\mathbf{r}}_{ab})$, namely,

$$\sigma(\omega_a, \omega_b, \hat{\mathbf{r}}_{ab}) = [2\hat{\mathbf{r}}_{ab}^T \mathbf{A}^{-1}(\omega_a, \omega_b) \hat{\mathbf{r}}_{ab}]^{-1/2}, \quad (3)$$

where the symmetric overlap matrix \mathbf{A} is defined as

$$\mathbf{A}(\omega_a, \omega_b) = \mathbf{M}^T(\omega_a) \mathbf{S}_a^2 \mathbf{M}(\omega_a) + \mathbf{M}^T(\omega_b) \mathbf{S}_b^2 \mathbf{M}(\omega_b), \quad (4)$$

and \mathbf{S}_i is the shape matrix with elements $S_{\alpha\beta}^{(i)} = \delta_{\alpha\beta} \sigma_{\alpha}^{(i)}$, where $\sigma_x^{(i)}$, and $\sigma_y^{(i)}$, and $\sigma_z^{(i)}$ are the three axes of each ellipsoidal fragment. The $\mathbf{M}(\omega_i)$ are rotation matrices connecting the laboratory to the fragment frame i . The interaction term is $\epsilon(\omega_a, \omega_b, \hat{\mathbf{r}}_{ab}) = \epsilon^\nu(\omega_a, \omega_b) \epsilon'^\mu(\omega_a, \omega_b, \hat{\mathbf{r}}_{ab})$, with μ and ν empirical exponents,¹⁷ and

$$\epsilon(\omega_a, \omega_b) = \left[\frac{2\sigma_e^{(a)} \sigma_e^{(b)}}{\det[\mathbf{A}(\omega_a, \omega_b)]} \right]^{1/2}, \quad (5)$$

with geometrical scaling constants $\sigma_e^{(i)} = [\sigma_x^{(i)} \sigma_y^{(i)} + \sigma_z^{(i)} \sigma_z^{(i)}] [\sigma_x^{(i)} \sigma_y^{(i)}]^{1/2}$, and

$$\epsilon'(\omega_a, \omega_b, \hat{\mathbf{r}}_{ab}) = 2\hat{\mathbf{r}}_{ab}^T \mathbf{B}^{-1}(\omega_a, \omega_b) \hat{\mathbf{r}}_{ab}. \quad (6)$$

The symmetric interaction matrix \mathbf{B} is

$$\mathbf{B}(\omega_a, \omega_b) = \mathbf{M}^T(\omega_a) \mathbf{E}_a \mathbf{M}(\omega_a) + \mathbf{M}^T(\omega_b) \mathbf{E}_b \mathbf{M}(\omega_b), \quad (7)$$

where the matrix \mathbf{E}_i with elements $E_{\alpha\beta}^{(i)} = \delta_{\alpha\beta} (\epsilon_0 / \epsilon_{\alpha\beta}^{(i)})^{1/\mu}$ contains the parameters $\epsilon_x^{(i)}$, and $\epsilon_y^{(i)}$, and $\epsilon_z^{(i)}$ proportional to the well depths for the *side-by-side*, *face-to-face*, and *end-to-end* interactions of the fragments.

In the biaxial Gay-Berne potential the interaction energy also depends on two tuning parameters μ , ν and the parameter σ_c which measures the width of the potential wells²² and has been computed as $\sigma_c = (1/2)[\sigma_c^{(a)} + \sigma_c^{(b)}]$ with $\sigma_c^{(i)} = \min\{\sigma_x^{(i)}, \sigma_y^{(i)}, \sigma_z^{(i)}\}$. Distances and interaction energies are scaled with respect to the chosen reference molecular units: σ_0 for distances, and ϵ_0 for energies.

III. MOLECULAR CHIRALITY PARAMETERS

Since our main task is to relate molecular chirality to phase organization, it is clearly essential to start by introducing a quantitative measure of molecular chirality. This is a deceptively simple task as it can be based on a variety of properties of interest and indeed there are a number of definitions in literature.²⁶ In general, these different definitions relate a chirality parameter to some third rank tensor which is nonzero in the absence of a symmetry center and that is relevant to the problem. In this work we follow the approach proposed by Nordio and co-workers²⁷ that describes chirality as a property connected to the molecular surface and shape. Applying this model to our chiral particles requires calculating the surface (\mathbf{T}) and the helicity (\mathbf{Q}) tensors²⁷ of the par-

ticle. The \mathbf{T} tensor, with elements $T_{\alpha\beta}$, describes how the surface S of an object, with local normal vector $\hat{\mathbf{s}}$, extends in space,

$$T_{\alpha\beta} = -\langle s_\alpha s_\beta \rangle = -\int_S dS s_\alpha s_\beta, \quad (8)$$

$$\text{Tr}[\mathbf{T}] = -S, \quad (9)$$

where the surface integral is carried out over the products of the components s_x , and s_y , and s_z of $\hat{\mathbf{s}}$ measured with respect to the molecular frame. On the other hand \mathbf{Q} is a second-rank pseudotensor with elements $Q_{\alpha\beta}$ related to the third-rank tensor $Q_{\alpha\beta\gamma}^{(3)}$ that describes how the surface orientation changes moving along the three directions of Cartesian space,²⁸

$$Q_{\alpha\beta\gamma}^{(3)} = -3\langle s_\alpha r_\beta s_\gamma \rangle \quad (10)$$

and

$$Q_{\alpha\beta} = -\frac{1}{3} \sum_{\gamma,\delta} \epsilon_{\alpha\gamma\delta} Q_{\gamma\delta\beta}^{(3)}, \quad (11)$$

where r_α are the components of the position vector of the surface element, and $\epsilon_{\alpha\beta\gamma}$ are the elements of the Levi-Civita tensor. Combining the diagonal components of these second-rank tensors Nordio and co-workers²⁷ have obtained a single pseudoscalar χ associated with the overall chirality of the surface

$$\chi = -1000(Q_{xx}T_{xx} + Q_{yy}T_{yy} + Q_{zz}T_{zz})/S^{5/2}. \quad (12)$$

From symmetry considerations it follows that χ vanishes for achiral systems. In addition, it has opposite sign for two enantiomers, as a consequence of the invariance of \mathbf{T} and the change of sign of \mathbf{Q} components. Finally, the normalizing factor $S^{5/2}$, makes the product independent of the actual extent of molecular surface S .

IV. PARAMETERIZATION OF THE CTS MODEL

Following the “decorated disk” idea, we have studied three model systems of different shape chirality. The first and simplest contains only a reference nonchiral system, formed by a squashed biaxial ellipsoid, with aspect ratios inspired by reference to substituted pyrenic core discotics like the molecule 1,3,6,8-tetrakis((S)-2-(heptiloxy)propanoyloxy)pyrene denominated $P4m^*10$.¹⁰ This mesogen, originally prepared by Boch and Helfrich,¹⁰ exhibits upon cooling from isotropic a chiral columnar phase from 307 K to 269 K where it becomes a crystal. This molecule is much too complicated, at least at this stage, for a realistic simulation but we adopt the dimensions of its central core comprising pyrene and propanoyloxy substituents for determining the axes of our reference ellipsoid. In practice, we have calculated the geometry of $P4m^*10$ at the Molecular Mechanics level using the COMPASS98.01 (Ref. 29) force field, and computed the ratios of the sides $b_x = 11.6 \text{ \AA}$, and $b_y = 15.89 \text{ \AA}$, and $b_z = 3.40 \text{ \AA}$ of a box enclosing the core obtaining $b_x/b_y = 0.73$, and $b_z/b_y = 0.214$. These ratios have been used to scale the biaxial ellipsoid axes to a volume equal to that of the uniaxial discotic particles used in previous studies.³⁰ We have used this system for a preliminary study in order to find the pa-

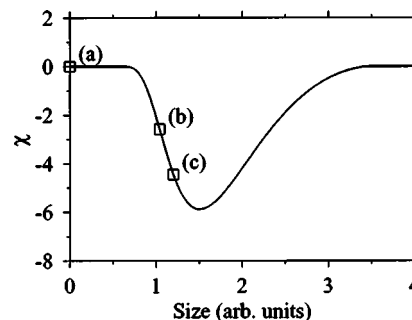


FIG. 2. The shape chiralities χ of the CTS models considered in this work (squares) as a function of the scale factor s used to dimension the second site (the units of s have been arbitrary chosen so that $s=1$ corresponds to model [b]). The continuous curve gives the value of χ as a function of s .

rameterization required to generate a stable nematic phase in a wide temperature range followed by a columnar phase at lower temperatures. This allows us to evaluate, by comparison with this reference, the effects of the chiral insertion.

Starting from this simple achiral oblate ellipsoid, we have developed two additional CTS models by embedding a second ellipsoidal site so that the particle acquires an overall dissymmetry (see Fig. 1). The position and orientation of the second site are fixed, and models with different shape chirality have been obtained by simply scaling the axes of the second site by a factor s .

The detailed description of the three models we have employed is as follows:

- Biaxial monosite achiral particle with σ_α axes $\sigma_x = 0.95 \sigma_0$, and $\sigma_y = 1.302 \sigma_0$, and $\sigma_z = 0.279 \sigma_0$, and interaction parameters $\epsilon_x = 0.55 \epsilon_0$, and $\epsilon_y = 0.367 \epsilon_0$, and $\epsilon_z = 2.2 \epsilon_0$. The ϵ_α coefficients have been chosen considering the interaction energy surface of two pyrene cores calculated using the Molecular Mechanics model described so far, and then by reducing by a factor 2.5 the ratio ϵ_z/ϵ_x and increasing by a factor 1.2 the ratio ϵ_z/ϵ_y in order to mimic the effect of the alkylic chains.
- CTS particle obtained with a type [a] particle transversally embedded with a second, smaller, biaxial disk which is weakly attractive, rotated and shifted from the center of the main site. We have chosen for its size $\sigma_x = 0.547 \sigma_0$, and $\sigma_y = 0.75 \sigma_0$, and $\sigma_z = 0.276 \sigma_0$, and for its interaction terms $\epsilon_x = 0.1 \epsilon_0$, and $\epsilon_y = 0.1 \epsilon_0$, and $\epsilon_z = 0.1 \epsilon_0$. The position of the tilted disk with respect to the origin of the main site is $X=0$, $Y=-0.35$, $Z=0$ while its orientation, in terms of Euler angles, is $\alpha=0^\circ$, $\beta=15^\circ$, and $\gamma=60^\circ$. The shape chirality parameter calculated for this model is $\chi = -2.08$, and the size of the second site has been associated to a scale factor $s=1$ (see Fig. 2).
- CTS chiral particle similar to the model [b] but characterized by a higher shape chirality. Model [c] is obtained by using a scaling factor $s=1.19927$ for the second disk, corresponding to $\sigma_x = 0.656 \sigma_0$, and $\sigma_y = 0.9 \sigma_0$, and $\sigma_z = 0.331 \sigma_0$. The shape chirality parameter for this model is $\chi = -4.455$.

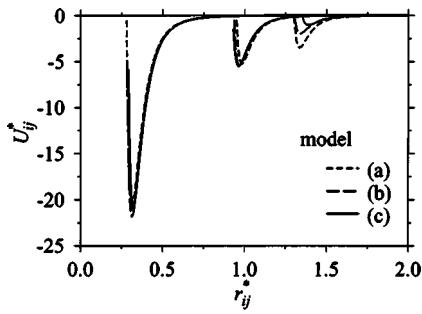


FIG. 3. The Gay–Berne energy for a pair of model [a] (short dashed), [b] (long dashed), and [c] (continuous) CTS particles as a function of center–center separation. The profiles for the *face-to-face*, *side-by-side*, and *end-to-end* configurations are those shown in order of increasing distance.

In addition, we have used in all cases $\mu=1$, and $\nu=3$ as model exponents for the GB potential. In Fig. 2 we report the theoretical curve for the shape chirality χ as a function of s together with the χ values for the model systems considered in this work. These values have been obtained by numerical integration on the particle surface using a grid of 22×400 elements and by following the prescription given by the authors of Refs. 27, 28 assuming a uniform density of mass for the overlapped ellipsoidal particles. In practice, we have worked in the coordinate system diagonalizing \mathbf{T} . For these CTS models we also employ the molecular units of length $\sigma_0=12 \text{ \AA}$, and of energy $\epsilon_0/k_B=100 \text{ K}$. The Gay–Berne energy profiles for the *face-to-face*, *side-by-side*, and *end-to-end* interactions for the three models are reported in Fig. 3. We see from the curves for models [b] and [c] that the presence of the transversal site does not appreciably affect the stronger *face-to-face*, and *side-by-side* curves and becomes relevant only for the weaker *end-to-end* interaction. Since the $\epsilon_\alpha^{(i)}$ coefficients for the transverse sites have been chosen to be relatively small compared to those of the main site, we conclude that the small chirality of our particles is essentially originating from their dissymmetric shape.

V. ORIENTATIONAL AND STRUCTURAL PROPERTIES

To study the nature of the orientational properties of the phases obtained it is essential to compute a set of single particle order parameters.^{25,31,32} In practice, the two most relevant ones for the present case, are the symmetrised second rank order parameters $\langle R_{00}^2 \rangle$ and $\langle R_{22}^2 \rangle$. They are defined as

$$\langle R_{00}^2 \rangle = \langle \frac{3}{2} (\hat{\mathbf{z}}_i \cdot \hat{\mathbf{Z}})^2 - \frac{1}{2} \rangle, \quad (13)$$

and

$$\langle R_{22}^2 \rangle = \langle \frac{1}{4} [(\hat{\mathbf{x}}_i \cdot \hat{\mathbf{X}})^2 - (\hat{\mathbf{x}}_i \cdot \hat{\mathbf{Y}})^2 - (\hat{\mathbf{y}}_i \cdot \hat{\mathbf{X}})^2 + (\hat{\mathbf{y}}_i \cdot \hat{\mathbf{Y}})^2] \rangle, \quad (14)$$

where $\hat{\mathbf{X}}$, and $\hat{\mathbf{Y}}$ and $\hat{\mathbf{Z}}$ are unit vectors defining the axes orientation of the mesophase director frame, and $\mathbf{a} \cdot \mathbf{b}$ represents a scalar vector product. The order parameters are computed from the eigenvalues of the three ordering matrices relative to the $\hat{\mathbf{x}}_i$, $\hat{\mathbf{y}}_i$, and $\hat{\mathbf{z}}_i$ molecular axes.³² We recall that $\langle R_{00}^2 \rangle$ corresponds to the standard $\langle P_2 \rangle$ order parameter of uniaxial phases measuring the average orientational order of

the molecular $\hat{\mathbf{z}}_i$ axis, and that it has a zero value in the isotropic phase. On the other hand $\langle R_{22}^2 \rangle$, which is different from zero only for biaxial molecules in biaxial phases, and has as maximum value $1/2$, is the largest and thus most useful biaxial order parameter³² and measures the difference in the average orientational order of the molecular $\hat{\mathbf{x}}_i$ and $\hat{\mathbf{y}}_i$ axes.

The mobility of the particles within the mesophase can be estimated by using an average mean square displacement,³³

$$\langle l_\alpha \rangle = \frac{1}{NM} \left[\sum_i^N \sum_n^M (r_{i,\alpha}^{(n)} - r_{i,\alpha}^{(0)})^2 \right]^{1/2}, \quad (15)$$

where $\mathbf{r}_i^{(n)} = \{r_{i,x}, r_{i,y}, r_{i,z}\}^{(n)}$ is the i th particle position with respect to the director frame with axes $\alpha = X$, or Y , or Z , after n of M Monte Carlo cycles, starting from an arbitrary point $\mathbf{r}_i^{(0)}$.

To determine the type of molecular organization of the ordered phases formed by our model particles we have computed various average pair correlation histograms. The first one we have considered is the distribution of centres of mass, i.e., the standard radial correlation function;

$$g_0(r) = \frac{1}{4\pi r^2 \rho} \langle \delta(r - r_{ij}) \rangle_{ij}, \quad (16)$$

where r is the radius of a spherical sampling region, ρ the number density, and the average $\langle \dots \rangle_{ij}$ is computed with respect to all molecular pairs.

The radial distribution in itself is not sufficient to characterize the columnar phases and their local anisotropy and biaxiality, so we have taken advantage of other pair correlation functions. In general we can resort to the expansion coefficients of the general pair distribution function $P^{(2)}(\omega_i, \omega_j, \mathbf{r}_{ij})$ which describes the positional-orientational correlations for a system with overall spherical symmetry, as in the case of a system with no external symmetry breaking field

$$g^{(2)}(\omega_i, \omega_j, \mathbf{r}_{ij}) = \frac{1}{\rho} \frac{P^{(2)}(\omega_i, \omega_j, \mathbf{r}_{ij})}{P^{(1)}(\omega_i)P^{(1)}(\omega_j)}, \quad (17)$$

where ω_i , and ω_j are the particle orientations, \mathbf{r}_{ij} is the intermolecular vector, and $P^{(1)}(\omega_i)$ is the one-particle orientational distribution. This pair correlation function can be expanded in an orthogonal basis of rotational invariant functions $S_{n_1 n_2}^{L_1 L_2 L_3}(\omega_i, \omega_j, \hat{\mathbf{r}}_{ij})$ (Ref. 31) as shown by Blum and Torruella³⁴ and Stone.³⁵ The expansion coefficients of the pair correlation are functions of intermolecular distance r and can be routinely computed during a simulation run as average histograms.³⁶

In particular, in this work we have characterized the local biaxial structure using the following orientational correlation functions,

$$\begin{aligned} \text{Re}[S_{22}^{220}](r) = & \frac{1}{4\sqrt{5}} \langle \delta(r-r_{ij}) ((\hat{\mathbf{x}}_i \cdot \hat{\mathbf{x}}_j)^2 - (\hat{\mathbf{x}}_i \cdot \hat{\mathbf{y}}_j)^2 \\ & - (\hat{\mathbf{y}}_i \cdot \hat{\mathbf{x}}_j)^2 + (\hat{\mathbf{y}}_i \cdot \hat{\mathbf{y}}_j)^2 - 2(\hat{\mathbf{x}}_i \cdot \hat{\mathbf{y}}_j)(\hat{\mathbf{y}}_i \cdot \hat{\mathbf{x}}_j) \\ & - 2(\hat{\mathbf{x}}_i \cdot \hat{\mathbf{x}}_j)(\hat{\mathbf{y}}_i \cdot \hat{\mathbf{y}}_j)) \rangle_{ij}, \end{aligned} \quad (18)$$

$$\begin{aligned} \text{Im}[S_{22}^{220}](r) = & \frac{2}{4\sqrt{5}} \langle \delta(r-r_{ij}) (-(\hat{\mathbf{x}}_i \cdot \hat{\mathbf{x}}_j)(\hat{\mathbf{x}}_i \cdot \hat{\mathbf{y}}_j) \\ & - (\hat{\mathbf{x}}_i \cdot \hat{\mathbf{x}}_j)(\hat{\mathbf{y}}_i \cdot \hat{\mathbf{x}}_j) + (\hat{\mathbf{x}}_i \cdot \hat{\mathbf{y}}_j)(\hat{\mathbf{y}}_i \cdot \hat{\mathbf{y}}_j) \\ & + (\hat{\mathbf{y}}_i \cdot \hat{\mathbf{x}}_j)(\hat{\mathbf{y}}_i \cdot \hat{\mathbf{y}}_j)) \rangle_{ij}. \end{aligned} \quad (19)$$

The function $\text{Re}[S_{22}^{220}](r)$ measures the average correlation, as a function of distance r , between like $\hat{\mathbf{x}}_i, \hat{\mathbf{x}}_j$ and $\hat{\mathbf{y}}_i, \hat{\mathbf{y}}_j$ pairs of axes, and it is directly related to the $\langle R_{22}^2 \rangle$ order parameter.³⁶ On the other hand, the correlation $\text{Im}[S_{22}^{220}](r)$ considers unlike pairs, e.g., $\hat{\mathbf{x}}_i$ and $\hat{\mathbf{y}}_j$.

These observables do not afford an assessment of the chirality of the columnar structures that follows, for instance, because of a helical distribution of centers of mass inside columns and a more specific analysis procedure is then given in the next section.

VI. ANALYSIS OF COLUMNAR STRUCTURES

A significant problem that has to be solved for the analysis of the simulation results (similarly to what would happen for a real sample) is that of recognizing if chiral columnar structures are formed when at sufficiently low temperatures, the system starts to self-organize. To understand how molecular chirality can perturb the organization of columnar aggregates we have, first of all, to extract these cylindrical structures from the sample. This is not trivial also because the type of columns, their length, and their polydispersity are not known *a priori*. Here, the determination of the columnar structure of a MC configuration has been accomplished by performing the following steps:

- Identification of columnar aggregates;
- Computation of columnwise chiral orientational correlations;
- Assessment of helical structures by means of a pair positional correlation;
- Comparison of results with those for model columnar structures;
- Study of chiral defects.

The results from steps (a) to (c) have been averaged over all configurations analyzed and used to build average histograms related to the whole sample. Further analyses have been necessary afterwards in order to understand the role played by defects.

The determination of the polydispersity of the distribution of columnar aggregates is the first problem we address. We adopt a purely particle–particle distance based algorithm to assign particles in the MC sample to columnar aggregates. In practice, every pair of molecules with distance r_{ij} smaller than a threshold r_t is considered as belonging to a column. By linking all pairs sharing common particles it is possible to

determine the composition of the columnar structures and, furthermore, to determine the average distribution of column lengths. The identification algorithm used to extract and analyze columnar structures from the MC configurations is described in Appendix A.

Having mapped the particles aggregates we wish to introduce some indicators of chiral correlation between molecules belonging to the same column. The chiral orientational correlations we have found useful are

$$S_{00}^{221}(r) = -\frac{\sqrt{3}}{\sqrt{10}} \langle \delta(r-r_{ij}) ((\hat{\mathbf{z}}_i \cdot \hat{\mathbf{z}}_j)(\hat{\mathbf{z}}_i \cdot \hat{\mathbf{z}}_j \times \hat{\mathbf{r}}_{ij})) \rangle_{ij}, \quad (20)$$

$$\begin{aligned} \text{Re}[S_{20}^{221}](r) = & \frac{1}{2\sqrt{5}} \langle \delta(r-r_{ij}) (-(\hat{\mathbf{x}}_i \cdot \hat{\mathbf{z}}_j)(\hat{\mathbf{x}}_i \cdot \hat{\mathbf{z}}_j \times \hat{\mathbf{r}}_{ij}) \\ & + (\hat{\mathbf{y}}_i \cdot \hat{\mathbf{z}}_j)(\hat{\mathbf{y}}_i \cdot \hat{\mathbf{z}}_j \times \hat{\mathbf{r}}_{ij})) \rangle_{ij}, \end{aligned} \quad (21)$$

$$\begin{aligned} \text{Re}[S_{2-2}^{221}](r) = & \frac{1}{2\sqrt{30}} \langle \delta(r-r_{ij}) (-(\hat{\mathbf{x}}_i \cdot \hat{\mathbf{x}}_j)(\hat{\mathbf{x}}_i \cdot \hat{\mathbf{x}}_j \times \hat{\mathbf{r}}_{ij}) \\ & - (\hat{\mathbf{x}}_i \cdot \hat{\mathbf{x}}_j)(\hat{\mathbf{y}}_i \cdot \hat{\mathbf{y}}_j \times \hat{\mathbf{r}}_{ij}) + (\hat{\mathbf{x}}_i \cdot \hat{\mathbf{y}}_j)(\hat{\mathbf{x}}_i \cdot \hat{\mathbf{y}}_j \times \hat{\mathbf{r}}_{ij}) \\ & - (\hat{\mathbf{x}}_i \cdot \hat{\mathbf{y}}_j)(\hat{\mathbf{y}}_i \cdot \hat{\mathbf{x}}_j \times \hat{\mathbf{r}}_{ij}) - (\hat{\mathbf{y}}_i \cdot \hat{\mathbf{x}}_j)(\hat{\mathbf{x}}_i \cdot \hat{\mathbf{y}}_j \times \hat{\mathbf{r}}_{ij}) \\ & + (\hat{\mathbf{y}}_i \cdot \hat{\mathbf{x}}_j)(\hat{\mathbf{y}}_i \cdot \hat{\mathbf{x}}_j \times \hat{\mathbf{r}}_{ij}) - (\hat{\mathbf{y}}_i \cdot \hat{\mathbf{y}}_j)(\hat{\mathbf{x}}_i \cdot \hat{\mathbf{x}}_j \times \hat{\mathbf{r}}_{ij}) \\ & - (\hat{\mathbf{y}}_i \cdot \hat{\mathbf{y}}_j)(\hat{\mathbf{y}}_i \cdot \hat{\mathbf{y}}_j \times \hat{\mathbf{r}}_{ij})) \rangle_{ij}. \end{aligned} \quad (22)$$

The imaginary parts (not reported here for the sake of concision) are also readily derived from their definition.³⁵ By inspection of the equations above, it is apparent that $S_{00}^{221}(r)$ measures the average chiral correlation between the molecular $\hat{\mathbf{z}}_i$, and $\hat{\mathbf{z}}_j$ axes (i.e., it is related to molecular tilt) at distance r . In a similar fashion, we find that $\text{Re}[S_{20}^{221}](r)$ gives information about cross-correlations between $\hat{\mathbf{x}}_i$, and $\hat{\mathbf{y}}_i$, and the $\hat{\mathbf{z}}_j$ axis (i.e., it estimates the coupling between molecular tilt and twist). Finally, $\text{Re}[S_{2-2}^{221}](r)$ relates the orientations of $\hat{\mathbf{x}}_i$, and $\hat{\mathbf{y}}_i$ with $\hat{\mathbf{x}}_j$, and $\hat{\mathbf{y}}_j$ axes and measures the molecular twist correlations. Similarly to what we have done for the biaxial orientational correlations we have computed average histograms of these chiral pair functions. In this case, though, we have adopted a cylindrical shaped sampling region and by using the aggregates provided by the identification algorithm, we have computed these histograms in a columnwise fashion.

The columnar structures might also exhibit a helical distribution of centres of mass of the particles (“*spirals*”) as proposed by Bock and Helfrich.¹⁰ Since the orientational chiral correlations do not depend on this feature, they cannot assess if such a roto-translational axis is present. We have then introduced to this purpose a more specialized two-dimensional histogram $P(r_{ij}, \alpha_{ij})$ which measures the average probability of finding a pair of particles of the aggregate at distance r_{ij} , and with projection twist angle α_{ij} with respect to the column axis $\hat{\mathbf{n}}_c$ (see Fig. 18 below). In presence of a helical distribution of the centers of mass a regular pattern in the maxima of $P(r_{ij}, \alpha_{ij})$ should emerge, and from the slope it should also be possible to determine the helical

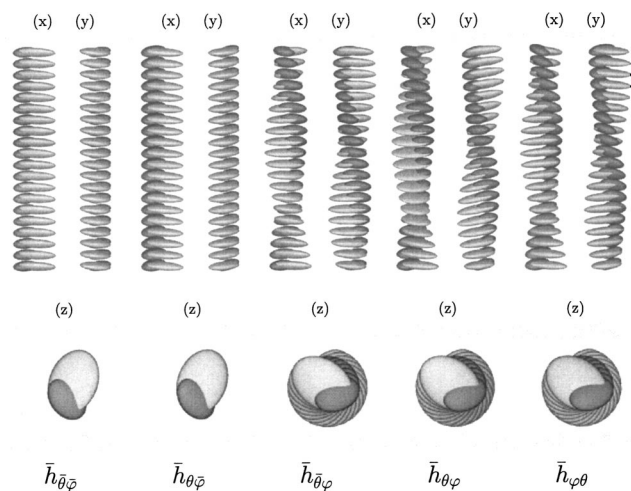


FIG. 4. Orthogonal views of nonhelical model columnar structures with $\theta = 0^\circ$, and $\theta = 10^\circ$, $\varphi = 0^\circ$, and $\varphi = -15^\circ$, and interparticle distance $r_{ij} = 0.36 \sigma_0$. For each structure we give the identifying label and show the lab-X, lab-Y, and lab-Z axes views of the molecular organization.

pitch of the distribution. The algorithm used for computing $P(r_{ij}, \alpha_{ij})$ is described in detail in Appendix B.

The various observables we have just introduced are in principle able to signal the presence of chirality in columnar structures but it is difficult to assess *a priori* their ability to discriminate between different types of columnar arrangements. It is thus useful to classify at least some of the idealized columnar structures that might arise. Without any attempt to develop a fully systematic description that would be beyond the scope of this work it is convenient to introduce a simple notation to help in the classification of these organizations. As described in Appendix C, here we use three symbols for labelling the different model columnar aggregates (see Figs. 4, and 5 for pictorial representations). In practice, the model structures can be used to identify which chiral correlations in Eqs. (20)–(22) (if any) can be used as a “fingerprint” for one of the column types of Figs. 4 and 5. In Table I we list, for the various structure types, a number of

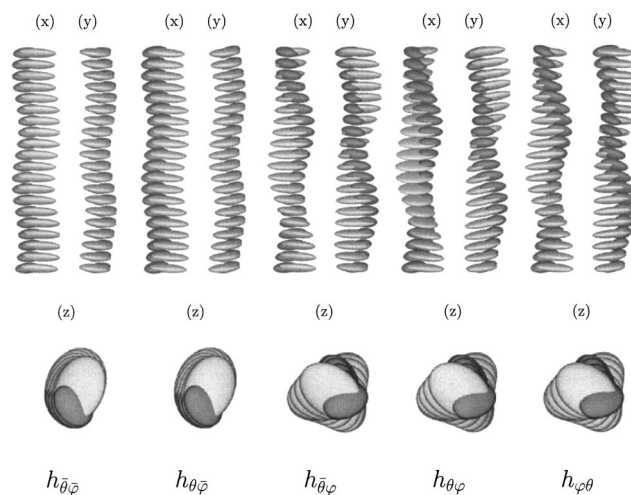


FIG. 5. Orthogonal views of helical model columnar structures with \hat{n}_c axis projection of the interparticle distance $z_{ij} = 0.36 \sigma_0$ and radius of the helical distribution $0.1 \sigma_0$. (See Fig. 4 for details.)

TABLE I. List of the columnwise chiral orientational correlations for the model columnar structures of Fig. 4 which are expected of being different from zero because of symmetry. The labels R, I stand for real and imaginary part.

	$\bar{h}_{\theta\bar{\varphi}}$	$\bar{h}_{\theta\bar{\varphi}}$	$\bar{h}_{\theta\varphi}$	$\bar{h}_{\theta\varphi}$	$\bar{h}_{\varphi\theta}$
S_{00}^{221}	R
S_{20}^{221}	R, I
S_{2-2}^{221}	I	I	R, I	R, I	R, I

correlations which are expected to be nonzero because of symmetry. We see, for instance, that if the only nonzero correlations were the real and the imaginary parts of $S_{2-2}^{221}(r)$ only the twisted nonspiraling columnar structures $\bar{h}_{\theta\bar{\varphi}}$ or $\bar{h}_{\theta\varphi}$ would be compatible with this finding. To further discriminate between the two structures one might compute additional correlation functions beyond those listed in Table I. It is also possible to perform more quantitative estimations of the structure by studying the pair distance dependence of the columnwise chiral correlations, since a variation in θ , with constant φ , affects the amplitude of the correlation function, while a variation in φ , with constant θ , changes the wavelength of the oscillations. This allows to estimate the average molecular tilt θ , and twist φ in the columns. We notice that all these considerations are valid if the supermolecular structures are regular and free from defects. The presence of irregularities or defects might modify the appearance of the correlation functions and thus an additional analysis would be necessary. We postpone the discussion of the effect of defects to the next section.

VII. MONTE CARLO SIMULATIONS

Turning now to our computer experimental work, we have simulated, using the MC technique, systems of $N = 1024$ CTS particles under isobaric–isothermal (MC-NPT) conditions.¹⁹ For each model [a]–[c] the starting configuration was a well equilibrated sample in the isotropic phase. The temperature dependence of the phase behavior was studied by performing a cooling-down sequence of Monte Carlo runs where for each dimensionless temperature $T^* = k_B T / \epsilon_0$ studied the simulation runs have been started from the final equilibrated configuration of the preceding temperature. The ranges of T^* studied encompass isotropic, nem-

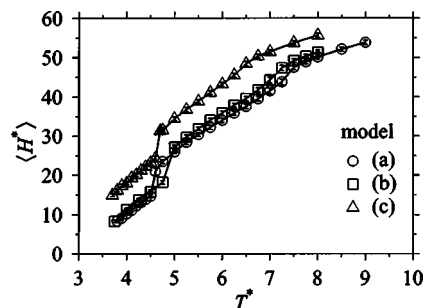


FIG. 6. The average enthalpy per particle $\langle H^* \rangle = (\langle U \rangle + P \langle V \rangle) / \epsilon_0$ as a function of temperature T^* for model systems [a] (circles), [b] (squares), and [c] (triangles). All MC simulations were run in the NPT ensemble at $P^* = 100$.

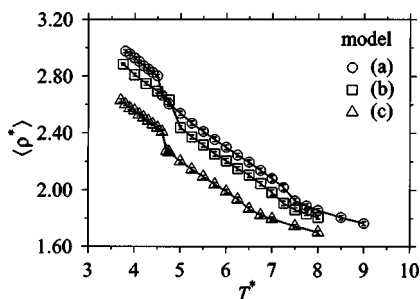


FIG. 7. The average number density $\langle \rho^* \rangle = N\sigma_0^3 \langle 1/V \rangle$ as a function of temperature T^* for model systems [a] (circles), [b] (squares), and [c] (triangles).

atic and columnar phases for all three models. We have employed a rectangular box with periodic boundary conditions and director axes parallel to the laboratory frame, and set a dimensionless pressure $P^* \equiv \sigma_0^3 P / \epsilon_0 = 100$ corresponding to ≈ 0.8 kbar. This relatively high value of P^* is necessary since we also wish to study the nematic phase of the discotic particles that disappears at lower pressures. The presence of a nematic is also more convenient from the simulation point of view in order to have a gradual change from the isotropic to columnar phase, thus reducing the chance that the system gets trapped in glassy configurations with macroscopic disorder and just locally ordered domains. We recall, however, that in real systems, including $P4m^*10$, the nematic is also normally absent at least at 1 atm. The box shape has been

allowed to change using a linear sampling of the volume $V^* \equiv V / \sigma_0^3$ by attempting to change the length of one randomly chosen simulation box side per time. We have adopted a pair potential cutoff radius $r_c = 4\sigma_0$, a Verlet neighbor list^{18,19} of radius $r_l = 5\sigma_0$, and the acceptance ratio for MC moves has been set to 0.4. Molecular orientations have been stored as quaternions.^{37,38} We have determined thermodynamic observables averaging over MC configurations sampled every 20 cycles, one cycle being a random sequence of N attempted single-particle MC moves. For all samples studied the equilibration runs were not shorter than 100 kcycles, with the production runs not shorter than 150–180 kcycles.

In Fig. 6 we plot the average enthalpy per particle $\langle H^* \rangle = (\langle U \rangle + P \langle V \rangle) / \epsilon_0$ as a function of temperature T^* . We see that for all three models [a]–[c] there are no appreciable discontinuities in the enthalpy in the higher range of temperatures corresponding to the isotropic–nematic (IN) transitions at temperature T_{IN}^* . A similar behavior can also be found for the number density $\langle \rho^* \rangle = N\sigma_0^3 \langle 1/V \rangle$, shown in Fig. 7, in agreement with the experimental finding that there are very small jumps of density in correspondence of the IN transition. A considerably different behavior has been found in the lower range of temperatures explored where both the enthalpy $\langle H^* \rangle$ and the density $\langle \rho^* \rangle$ have a small but well defined discontinuity across the nematic–columnar (NC) transition at T_{NC}^* . The average values of thermodynamical properties for the three models are reported in Tables II–IV.

TABLE II. The temperature T^* , average enthalpy $\langle H^* \rangle$, and energy $\langle U^* \rangle$ per particle, number density $\langle \rho^* \rangle$, and biaxial second rank orientational order parameters $\langle R_{00}^2 \rangle$, and $\langle R_{22}^2 \rangle$ for the system of $N=1024$ monosite biaxial achiral model [a] particles. All averages were computed by sampling one configuration each 20 MC cycles over NPT production runs of average length $N_p = 150$ –180 kcycles at pressure $P^* = 100$. The equilibration runs length N_e in all cases were not shorter than $N_p = 100$ kcycles. The root mean square errors are also reported.

T^*	$\langle H^* \rangle$	$\langle U^* \rangle$	$\langle \rho^* \rangle$	$\langle R_{00}^2 \rangle$	$\langle R_{22}^2 \rangle$
3.80	8.409 ± 0.339	−25.205 ± 0.247	2.975 ± 0.010	0.972 ± 0.000	0.051 ± 0.018
3.90	9.126 ± 0.396	−24.705 ± 0.283	2.956 ± 0.013	0.971 ± 0.002	0.044 ± 0.018
4.00	10.213 ± 0.321	−23.944 ± 0.217	2.928 ± 0.011	0.968 ± 0.000	0.032 ± 0.012
4.10	11.087 ± 0.403	−23.372 ± 0.281	2.902 ± 0.010	0.966 ± 0.001	0.044 ± 0.016
4.20	12.239 ± 0.369	−22.599 ± 0.254	2.870 ± 0.012	0.964 ± 0.002	0.037 ± 0.014
4.30	13.139 ± 0.520	−21.972 ± 0.355	2.848 ± 0.015	0.961 ± 0.001	0.029 ± 0.012
4.40	13.926 ± 0.371	−21.474 ± 0.257	2.825 ± 0.011	0.959 ± 0.002	0.021 ± 0.010
4.50	14.698 ± 0.390	−21.002 ± 0.267	2.801 ± 0.011	0.956 ± 0.002	0.016 ± 0.009
4.60	20.934 ± 0.921	−16.604 ± 0.666	2.664 ± 0.020	0.933 ± 0.005	0.019 ± 0.010
4.75	23.458 ± 0.522	−14.955 ± 0.339	2.603 ± 0.015	0.921 ± 0.004	0.019 ± 0.010
5.00	25.923 ± 0.480	−13.486 ± 0.305	2.538 ± 0.014	0.904 ± 0.006	0.015 ± 0.008
5.25	28.381 ± 0.502	−12.141 ± 0.291	2.468 ± 0.016	0.882 ± 0.007	0.016 ± 0.008
5.50	30.361 ± 0.464	−11.133 ± 0.250	2.410 ± 0.017	0.867 ± 0.009	0.015 ± 0.008
5.75	32.204 ± 0.525	−10.280 ± 0.258	2.354 ± 0.017	0.842 ± 0.011	0.015 ± 0.008
6.00	33.993 ± 0.540	−9.496 ± 0.266	2.300 ± 0.017	0.816 ± 0.014	0.015 ± 0.008
6.25	35.854 ± 0.490	−8.690 ± 0.238	2.245 ± 0.013	0.787 ± 0.015	0.014 ± 0.008
6.50	37.532 ± 0.561	−8.025 ± 0.260	2.195 ± 0.017	0.758 ± 0.016	0.014 ± 0.008
6.75	39.523 ± 0.564	−7.257 ± 0.243	2.138 ± 0.017	0.710 ± 0.019	0.014 ± 0.007
7.00	41.504 ± 0.750	−6.543 ± 0.292	2.082 ± 0.022	0.652 ± 0.036	0.013 ± 0.008
7.25	43.796 ± 0.688	−5.743 ± 0.262	2.019 ± 0.020	0.560 ± 0.042	0.012 ± 0.007
7.50	47.503 ± 0.624	−4.470 ± 0.245	1.924 ± 0.017	0.232 ± 0.075	0.009 ± 0.006
7.75	48.884 ± 0.514	−4.071 ± 0.196	1.889 ± 0.014	0.144 ± 0.044	0.008 ± 0.006
8.00	50.121 ± 0.495	−3.738 ± 0.196	1.857 ± 0.013	0.102 ± 0.033	0.007 ± 0.005
8.50	52.121 ± 0.548	−3.240 ± 0.199	1.806 ± 0.015	0.073 ± 0.027	0.008 ± 0.005
9.00	53.815 ± 0.564	−2.869 ± 0.195	1.764 ± 0.015	0.067 ± 0.023	0.008 ± 0.005

TABLE III. The average observables for the system of $N=1024$ CTS model [b] particles. (see Table II for computational details.)

T^*	$\langle H^* \rangle$	$\langle U^* \rangle$	$\langle \rho^* \rangle$	$\langle R_{00}^2 \rangle$	$\langle R_{22}^2 \rangle$
3.75	8.340±0.333	-26.329±0.238	2.884±0.007	0.963±0.000	0.066±0.012
4.00	11.353±0.354	-24.235±0.242	2.810±0.011	0.956±0.002	0.017±0.010
4.25	13.714±0.443	-22.682±0.293	2.748±0.012	0.949±0.002	0.021±0.011
4.50	15.825±0.440	-21.302±0.289	2.693±0.013	0.943±0.002	0.020±0.010
4.75	18.172±0.447	-19.817±0.295	2.632±0.012	0.935±0.003	0.017±0.009
5.00	27.171±0.492	-13.855±0.302	2.438±0.013	0.885±0.006	0.015±0.008
5.25	29.724±0.537	-12.437±0.323	2.372±0.015	0.863±0.009	0.015±0.008
5.50	31.845±0.467	-11.333±0.258	2.316±0.014	0.845±0.009	0.014±0.008
5.75	34.080±0.493	-10.302±0.242	2.253±0.015	0.813±0.014	0.014±0.007
6.00	35.853±0.567	-9.501±0.284	2.205±0.016	0.783±0.017	0.013±0.007
6.25	37.894±0.491	-8.619±0.245	2.150±0.013	0.745±0.015	0.014±0.008
6.50	39.553±0.529	-7.966±0.248	2.105±0.015	0.715±0.019	0.013±0.007
6.75	41.793±0.567	-7.105±0.251	2.045±0.015	0.636±0.034	0.012±0.007
7.00	44.246±0.743	-6.212±0.299	1.982±0.020	0.529±0.048	0.012±0.007
7.25	47.335±0.671	-5.126±0.274	1.906±0.017	0.272±0.091	0.009±0.006
7.50	49.207±0.512	-4.544±0.210	1.861±0.013	0.113±0.045	0.008±0.005
7.75	50.319±0.473	-4.246±0.198	1.833±0.012	0.104±0.044	0.008±0.005
8.00	51.383±0.493	-3.954±0.202	1.807±0.012	0.080±0.031	0.008±0.005

In Fig. 8 we show the plots of $\langle R_{00}^2 \rangle$ and we see that all systems produce one or more orientationally ordered phases. The first transition is from the isotropic to the uniaxial nematic phase and it is characterized by a well pronounced change of $\langle R_{00}^2 \rangle$, while the corresponding plot of $\langle R_{22}^2 \rangle$ (not shown here for the sake of conciseness) shows no significant deviations from an average zero value. The uniaxial nematic phase is stable over a wide range of temperatures, until a second, albeit smaller, change of $\langle R_{00}^2 \rangle$ takes place in correspondence of the nematic to columnar phase transition, also signalled by the enthalpy and density. The jump of the order parameter is negligible for models [a] and [b] and very lim-

ited for model [c]. At low temperatures all columnar phases exhibit a rather small but nonzero phase biaxiality. The detailed nature of these phase transitions has not been further investigated since this would require a much larger sample. To evaluate the phase transition temperatures we have fitted the temperature dependencies of the $\langle R_{00}^2 \rangle$ order parameter (see Fig. 8) with a spline polynomial of third rank.³⁹ The transition temperatures, T_{IN}^* , and T_{NC}^* reported in Table V, are those corresponding to the maxima of the numerical derivatives of these spline polynomials.

In Fig. 9 we show the estimated mean square displacements $\langle l_\alpha \rangle$. We notice that these values are rather small, even

TABLE IV. The average observables for the system of $N=1024$ CTS model [c] particles. (see Table II for computational details.)

T^*	$\langle H^* \rangle$	$\langle U^* \rangle$	$\langle \rho^* \rangle$	$\langle R_{00}^2 \rangle$	$\langle R_{22}^2 \rangle$
3.70	14.942±0.326	-23.088±0.215	2.630±0.011	0.954±0.003	0.070±0.010
3.80	16.158±0.332	-22.284±0.222	2.601±0.011	0.951±0.002	0.063±0.009
3.90	17.296±0.368	-21.561±0.228	2.574±0.012	0.947±0.003	0.066±0.009
4.00	17.929±0.407	-21.178±0.274	2.557±0.011	0.946±0.002	0.064±0.009
4.10	19.284±0.374	-20.252±0.237	2.529±0.011	0.942±0.002	0.038±0.010
4.20	20.099±0.379	-19.753±0.254	2.509±0.015	0.939±0.003	0.038±0.011
4.30	21.147±0.416	-19.095±0.271	2.485±0.010	0.935±0.004	0.036±0.010
4.40	22.161±0.439	-18.485±0.278	2.460±0.010	0.930±0.004	0.034±0.010
4.50	23.181±0.447	-17.860±0.285	2.437±0.011	0.925±0.003	0.034±0.012
4.60	24.324±0.532	-17.179±0.335	2.410±0.013	0.920±0.005	0.038±0.010
4.70	31.266±0.514	-12.712±0.317	2.274±0.014	0.863±0.009	0.015±0.008
4.75	31.518±0.612	-12.603±0.370	2.267±0.014	0.859±0.012	0.015±0.008
5.00	34.453±0.471	-10.993±0.263	2.200±0.013	0.829±0.009	0.014±0.008
5.25	36.748±0.542	-9.860±0.282	2.146±0.014	0.794±0.015	0.014±0.008
5.50	38.859±0.466	-8.894±0.249	2.094±0.012	0.757±0.015	0.013±0.007
5.75	41.110±0.503	-7.924±0.246	2.039±0.013	0.702±0.018	0.014±0.008
6.00	43.191±0.488	-7.082±0.232	1.989±0.013	0.639±0.027	0.012±0.007
6.25	45.466±0.525	-6.242±0.237	1.934±0.014	0.547±0.028	0.011±0.007
6.50	48.406±0.588	-5.171±0.246	1.867±0.013	0.275±0.085	0.009±0.006
6.75	50.333±0.481	-4.538±0.203	1.823±0.012	0.125±0.051	0.008±0.006
7.00	51.476±0.474	-4.210±0.200	1.796±0.012	0.106±0.038	0.008±0.006
7.50	53.720±0.472	-3.610±0.196	1.744±0.011	0.082±0.031	0.008±0.005
8.00	55.652±0.516	-3.137±0.197	1.701±0.013	0.069±0.024	0.008±0.005

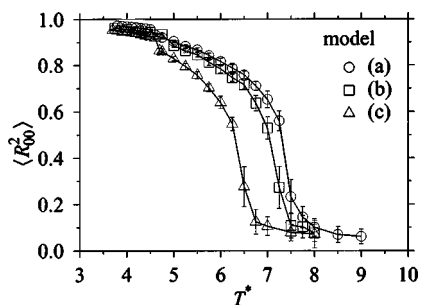


FIG. 8. The average orientational order parameter $\langle R_{00}^2 \rangle$ as a function of temperature T^* for model systems [a] (circles), [b] (squares), and [c] (triangles).

in the isotropic phase, as an effect of the high density of the sample. Entering the ordered phases the mobility along the \hat{Z} director axis becomes smaller than that along \hat{X} and \hat{Y} . This is expected on the grounds of the discotic shape of our molecules. In the columnar region the mean square displacements along \hat{X} , and \hat{Y} remain equal, showing that the mobility along a direction transversal to the columns axes is uniaxial, and the disposition of adjacent stacks is not biaxial.

In Fig. 10 we compare the radial distribution functions $g_0(r)$ for the three model systems for columnar phases with comparable $T^*/T_{NC}^* \approx 0.82$ scaled temperature. Differences in the radial correlation functions are small but significant, at least between the achiral model [a] and the chiral models [b], and [c]. In particular, we see that the columns formed by achiral [a] particles are well formed structures, that lead to sharply defined features in the radial correlation. Models [b], and [c] give practically the same $g_0(r)$, with profiles similar to that of model [a] but with more smeared characteristics. The first two peaks of the radial correlation function are relative to pairs belonging to the same columnar aggregate, while the hump corresponding to the range $r \approx 1 - 1.3\sigma_0$, also contains information on adjacent columns. Since these peaks are superimposed it is difficult to infer from them what is the organization of adjacent columns. However, a visual inspection shows that on average, the lattice has an hexagonal symmetry (see Fig. 13), and in spite of the particles being biaxial, we do not observe any rectangular packing of columns, even at the lowest temperatures. What we do observe is a small interdigitation of columns, especially for the chiral model [b] and, to a smaller extent, model [c]. This might in part explain the broader features of $g_0(r)$ when compared with that of model [a]. In the nematic phase the three models produce organizations with very similar $g_0(r)$ correlations (results not shown here).

TABLE V. The isotropic–nematic (IN) and nematic–columnar (NC) phase transition temperatures for the three models studied in this work.

Model	T_{IN}^*	T_{NC}^*
[a]	7.39	4.58
[b]	7.15	4.88
[c]	6.41	4.65

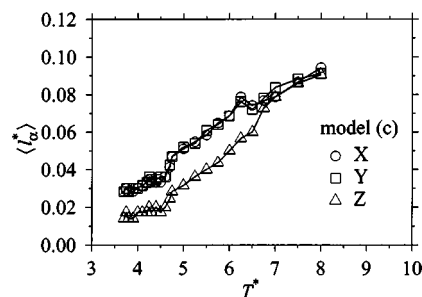


FIG. 9. The average molecular mean square displacement $\langle l_\alpha \rangle$ along the $\alpha = X$ (squares), Y (circles) or Z (triangles) axes of the director frame for model [c] system.

Moving from radial to orientational correlations, we see in Fig. 11 that the real part of the $S_{22}^{220}(r)$ histogram indicating the local biaxiality stemming from the correlation of \hat{x}_i and \hat{x}_j axes is significantly nonzero in the columnar phase of model [a], where particles can easily pile one over each other with their transversal axes aligned. If we consider a typical columnar stacked structure, this biaxial correlation extends on average over a range $\approx 1\sigma_0$, roughly corresponding to a stack of 3 molecules. On the other hand, the imaginary part of $S_{22}^{220}(r)$ is nonzero in the columnar phase of models [b], and especially [c] where the molecular twist gives rise to a nonzero average correlation between \hat{x}_i , and \hat{y}_j axes (see Fig. 12). The range of this correlation is again $\approx 1\sigma_0$. In the absence of a supermolecular columnar structure these effects become considerably smaller and short-ranged, as we observe in the nematic phases where they are practically restricted to the first neighbor (results not shown here). It should be noted though that $S_{22}^{220}(r)$ measures small orientational correlations and that it is usually a fairly noisy histogram, so quantitative conclusions from the plots of Figs. 11 and 12 should be taken with care.

Since model [c] is endowed with the highest chirality, we will devote most of our remaining discussion to the MC simulation results for this system trying to analyze its columnar structure and twist propagation. In Fig. 13 we show a snapshot of a, highly ordered, low temperature configuration of model [c] particles. The columnar structure is quite evident as well as the hexagonal packing of adjacent columns, but it is difficult to observe in a single configuration well defined

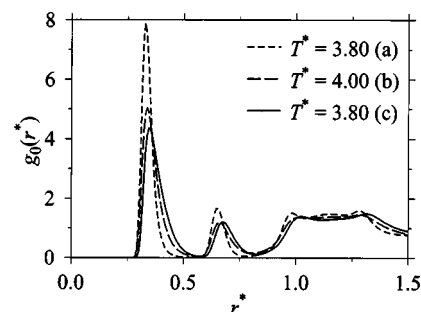


FIG. 10. The radial correlation function $g_0(r)$ for models [a] (short dashed), [b] (long dashed), and [c] (continuous) relative to columnar phases with similar scaled temperature $T^*/T_{NC}^* \approx 0.82$. Error bars have been omitted to avoid cluttering the plot.

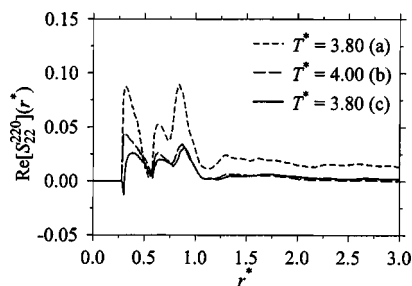


FIG. 11. The real part of the biaxial orientational correlation $S_{22}^{220}(r)$ for columnar phases of models [a] (short dashed), [b] (long dashed), and [c] (continuous). (See Fig. 10 for details.)

structural features which might account for the average biaxial properties measured by the orientational correlation functions discussed so far.

We now turn to identifying the columns and their polydispersity considering a typical configuration. The distance threshold r_t plays a key role in the column identification algorithm: if r_t is too small one might overlook significant nondensely packed structures (e.g., spatial helices or tilt-twist coupled columns); on the other hand, if r_t is comparable (or larger) than the average diameter of columnar structures the selection process could collapse neighboring columns into a single aggregate giving misleading results. In practice, r_t has been adjusted by trial and error in order to select all physically meaningful organized structures. As a rule of thumb for discotic mesogens, reasonable lower and upper bounds for the range of r_t are the minimum contact distances relative to all “face-to-face” and “edge-to-edge” configurations. In our case, an $r_t = 0.55\sigma_0$ was chosen in order to allow the extraction of more information and to gain a deeper insight of the structure of our ordered phases by effectively identifying doublets and triplets of particles. Using this threshold, the distribution of column lengths for a typical highly ordered columnar configuration of model [c] at $T^* = 3.7$ is shown in Fig. 14. We observe a dominant population of columns of length comparable to the simulation box side. In particular, the population of stacks extending across the whole MC sample is $\approx 65\%$ of the total. This is consistent with the intuitive physical picture of Fig. 13 of highly ordered columnar stacks extending throughout the entire sample.

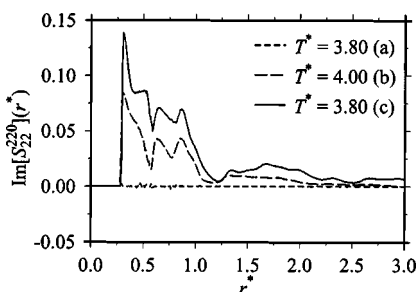


FIG. 12. The imaginary part of the biaxial orientational correlation $S_{22}^{220}(r)$ for columnar phases of models [a] (short dashed), [b] (long dashed), and [c] (continuous). (See Fig. 10 for details.)

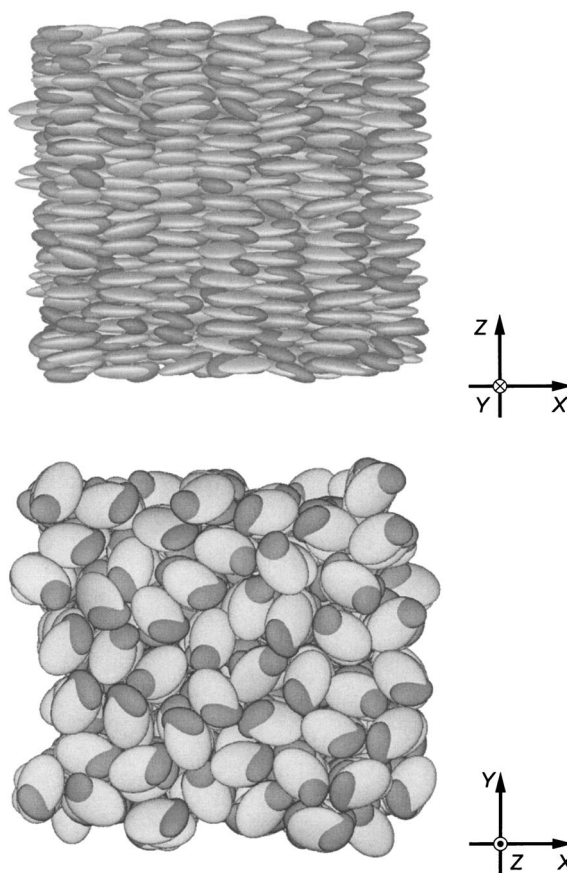


FIG. 13. Snapshots of typical MC configuration for the columnar phase of model [c] particles at $T^* = 3.7$. Views from the Y (top) and Z (bottom) directions of the director frame are shown.

In Figs. 15–17 we see the plots of the chiral correlations for the three systems studied in this work at similar scaled T^*/T_{NC}^* temperatures. The curve for model [a] is shown just as a check on numerical errors, and as expected from symmetry considerations it averages to zero. The plots for model [b] and [c] show the presence of a net overall chirality of the MC sample. Particularly for model [c], Fig. 15 reveals a clearly defined tilt coupling between \hat{z}_i axes that extends along the columns without changing sign for a range of $\approx 1.5\sigma_0$. This behavior is observed for all columnar samples, both close to, and well below the T_{NC}^* temperature, with the range of chiral correlation increasing with the de-

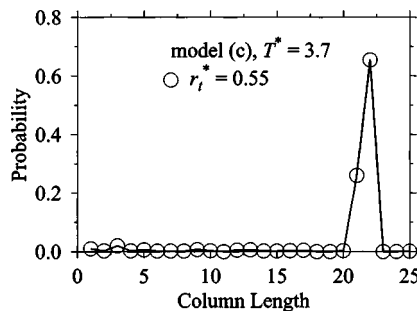


FIG. 14. The distribution of column length probability for a single configuration of model [c] particles at temperature $T^* = 3.7$. The threshold distance is $r_t = 0.55\sigma_0$.

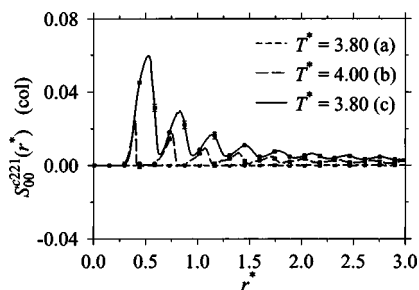


FIG. 15. The $S_{00}^{221}(r)$ chiral orientational correlation (computed columnwise as described in the text) for columnar phases of models [a] (short dashed), [b] (long dashed), and [c] (continuous) with similar scaled temperature $T^*/T_{NC}^* \approx 0.82$. Error bars have been plotted every 20 histogram bins.

crease in temperature. The molecular coupling between tilt and twist is not extremely large but unambiguous from the cross-correlation $\text{Re}[S_{20}^{221}](r)$ plotted in Fig. 16. The range is similar to that of $S_{00}^{221}(r)$, and for both these functions we notice fairly small error bars. This observation is consistent with the picture of average properties that are common to all configurations produced by the MC simulation. On the other hand, Fig. 17 shows that the twist correlation is much more noisy and short-ranged than the previous two and significant only between first neighboring pairs. For larger separations it decreases quite rapidly and becomes of the same order of magnitude of its fluctuations. Since this correlation is so short-ranged this result suggests that our chiral samples do not possess a regular distribution of twist angles propagating along the columnar axes such as those depicted for models dispositions in Fig. 4. We have tested the effect of periodic boundary conditions on these results by performing a MC simulation (150 kcycles long) at a selected temperature ($T^*=4.10$) on a much larger sample of $N=8192$ model [c] particles and finding essentially the same results for all observables and the chiral correlation functions $S_{00}^{221}(r)$, $S_{20}^{221}(r)$, and $S_{2-2}^{221}(r)$.

Having ruled out the simple twisted column structure we have considered helical aggregates. In Fig. 18 (top plate), we show the histogram $P(r_{ij}, \alpha_{ij})$ computed for two model helical structures with radius of the distribution $0.1\sigma_0$ and pitches $3.6\sigma_0$, and $7.2\sigma_0$. We observe that the pitch of the distribution can be clearly identified from the slope of the contour plots for the model structures, but not its radius. In Fig. 18 (bottom plate) we show the average histogram $P(r_{ij}, \alpha_{ij})$ computed for a highly ordered columnar phase of

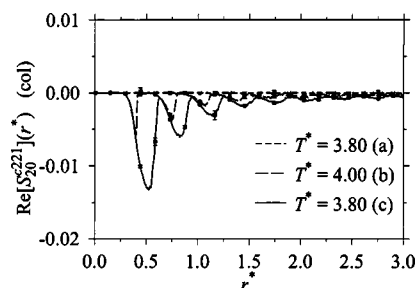


FIG. 16. The real part of the chiral orientational correlation $S_{20}^{221}(r)$ for columnar phases of models [a] (short dashed), [b] (long dashed), and [c] (continuous). (See Fig. 15 for details.)

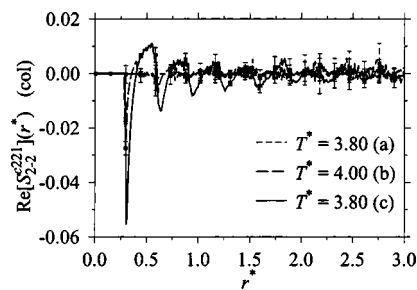


FIG. 17. The real part of the chiral orientational correlation $S_{2-2}^{221}(r)$ for columnar phases of models [a] (short dashed), [b] (long dashed), and [c] (continuous). (See Fig. 15 for details.)

model [c]. We see that the distribution is essentially isotropic, so we conclude that there is also no overall helical structure in this sample. Similar distributions have been found at all temperatures studied of models [b] and [c].

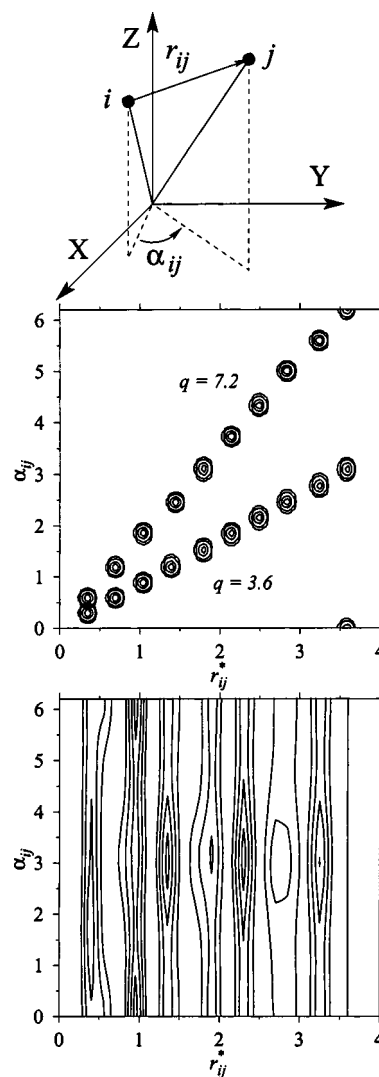


FIG. 18. Contour plots of the distributions $P(r_{ij}, \alpha_{ij})$ computed using the algorithm of Appendix B for (top plate) a model column of [c] particles with structure h_{θ_e} , and (bottom plate) average of the MC simulation of model [c] particles at $T^*=3.7$. The top plate contours are for columnar structures with projection distance $d_n=0.36\sigma_0$, and helical distribution of centers of mass with radius $0.1\sigma_0$ and pitches $q=3.6\sigma_0$, and $q=7.2\sigma_0$. The contours correspond to isolines at $P(r_{ij}, \alpha_{ij})=0.02, 0.04, 0.06, 0.08, 0.10$.

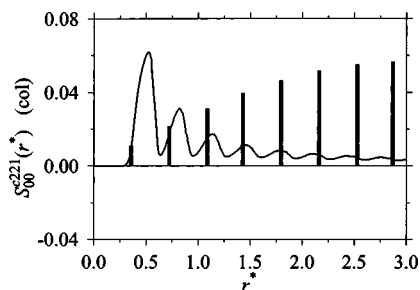


FIG. 19. Comparison of the columnwise chiral correlation $S_{00}^{221}(r)$ for system [c] at $T^* = 3.70$ (see Fig. 15) plotted as a continuous line, and that for model $\bar{h}_{\varphi\theta}$ with $\theta = 20^\circ$, and $\varphi = -10^\circ$ plotted as impulses (interparticle distance is $r_{ij} = 0.36\sigma_0$).

Continuing our analysis, we notice that in the case of chiral systems [b] and [c] all average columnwise chiral correlations computed in the columnar phases are nonzero (see Figs. 15–17, the imaginary components being not reported for simplicity). This finding would sort out the model structure $\bar{h}_{\varphi\theta}$ of Fig. 4 as the only candidate for the description of the simulated columnar mesophases. On the other hand, if we compare the average correlation resulting from the simulation of model [c] at $T^* = 3.70$ (see Fig. 15) with one computed for model $\bar{h}_{\varphi\theta}$ with $\theta = 20^\circ$, and $\varphi = -10^\circ$ and $r_{ij} = 0.36\sigma_0$ (see Fig. 19) we see that even if the absolute maxima of the two correlations have comparable heights, the sequence of maxima as function of the distance is completely mismatched. This behavior is quite general and even after optimizing the values of θ , and φ it was not possible to identify a model structure with a decreasing sequence similar to those of Fig. 15. Taking into account model structures with one or more randomly selected upside down particles, was also not helpful for the interpretation of the simulations results. Giving up a sample wide approach we have then performed a systematic analysis of single columns and we have tried to identify structural features that are common between most of the aggregates and that could be responsible of the average behavior of Fig. 15. To do so, we have chosen the lowest temperature sample of model [c] as the candidate columnar phase with larger chirality effects and correlations. We have found (see Fig. 20) that the column dissymmetry is indeed not originating from a uniform chiral arrangement of particles but seems to be mainly due to one-particle high-chirality defects separated by low-chirality and low-biaxiality domains. In Fig. 20, we see an example of such structures which is representative of the whole sample. Particle #14 has a larger tilt than its neighbors and this accounts for: (a) large short-range chiral correlation, and (b) smaller long-range chiral correlation with other particles (up to five molecular dimensions, shown as thick spikes in Fig. 20). In addition, we can see from the column snapshot, on top of Fig. 20, that most molecules are arranged in biaxial clusters of two or three particles that do not contribute to the overall column chirality. Since these molecules possess a small tilt θ their contribution to the magnitude of the correlation $S_{00}^{221}(r)$ is small, and it is not possible to characterize precisely the chiral features of these clusters. We conclude that the long range chiral correlations are originating from high chirality

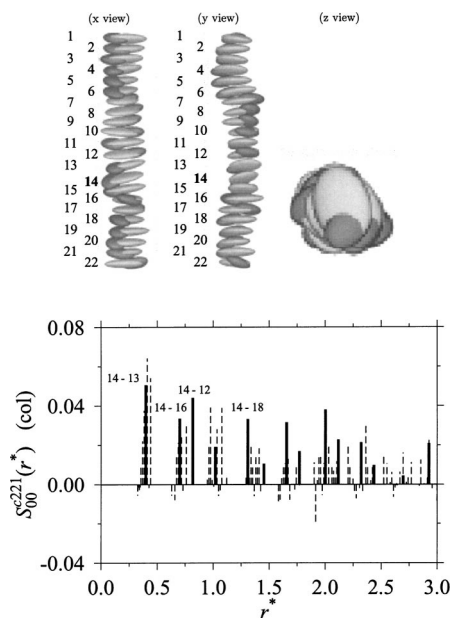


FIG. 20. Example of single-column structural analysis for an aggregate structure of system [c] at $T^* = 3.70$. Top row, from left to right: lab-X, lab-Y, and lab-Z axes views of a column extracted from a MC configuration. Bottom plate, plot of $S_{00}^{221}(r)$ computed for all pairs in the columnar structure (dashed impulses). The lines relative to the defect particle #14, showing the long range chiral correlation are shown as thick impulses.

centers separated by low chirality regions. Using this result, it is possible to analyze the chiral correlation functions at other temperatures and compare them with those computed for the model columnar structures. The results of our analyses for the MC simulations of model [c] can be summarized as follows. At low temperature the columnar mesophases are highly ordered and the high chirality centers are formed by molecules with large tilt $\theta \approx 20^\circ - 25^\circ$, twist $\varphi \approx 20^\circ - 30^\circ$ and chiral correlation with neighboring molecules. These centers are separated by low chirality regions formed by stacks of molecules with small tilt $\theta < 10^\circ$, twist $\varphi \approx 10^\circ$ and biaxiality. At higher temperature and lower orientational order the columnar mesophases exhibit chirality centers formed by molecules with tilt $\theta \approx 15^\circ - 20^\circ$ and twist $\varphi \approx 20^\circ - 30^\circ$. Again, these centers are separated by low-chirality stacks of molecules with tilt $\theta < 10^\circ$, twist $\varphi \approx 10^\circ$, and small biaxiality. These features are associated to molecular structures that have a small energy difference with respect to achiral ones. According to this interpretation the columns are stable entities but their detailed chiral structure is not. The columnar organization fluctuates in the course of the simulation when chiral and achiral arrangements of particles are continuously generated by the Monte Carlo configuration space sampling algorithm.

VIII. CONCLUSIONS

We have analyzed the effects of molecular dissymmetry of chiral two-sites molecules on the structure and chirality of the liquid crystal columnar organization they form. The columnar systems show an overall average phase chirality and we observe a coupling between molecular tilt and twist between pairs of molecules within the same columnar structure.

The centers of mass do not describe a spatial helix and we find that it is not possible to analyze the simulation results in terms of a continuous modulation of tilt and twist along columns.

For our CTS system with highest shape dissymmetry, the column chirality is not originating from a regular arrangement of particles but seems to be mainly due to one-particle high-chirality defects separated by low-chirality low-biaxiality domains. These structures have a small thermodynamic stability and undergo a continuous formation and destruction during the evolution of the Monte Carlo simulation. Although this study highlights that the complexity of chiral organizations is much greater than the simple idealized pictures shown, e.g., in Figs. 4 and 5, we believe the tools we have developed and described will be of use in an improved description of molecular level experiments and simulations as they become available.

ACKNOWLEDGMENTS

We thank MIUR PRIN *Cristalli Liquidi*, University of Bologna, and EU TMR contract No. FMRX-CT97-0121 for financial support, and Dr. D. Blunk (Köln), Professor R. Memmer (Kaiserslautern), and Professor J.L. Serrano (Zaragoza) for stimulating discussions.

APPENDIX A: COLUMN IDENTIFICATION PROCEDURE

In this Appendix, we describe the column identification procedure we have used to extract stacks of particles from the MC configurations. The algorithm proceeds in two sweeps. The first is performed by looping over all distinct molecular pairs as follows:

- (1) A molecule i is chosen; if the molecule does not already belong to a stack it is assigned a new structure label;
- (2) A second molecule $j > i$ is selected. If $r_{ij} < r_t$ molecule j is considered belonging to the same stack containing molecule i ;
- (3) Points (1) and (2) are repeated until all pairs have been considered.

After completion of the first sweep all stacks formed by triplets and doublets of particles will have been identified and labeled (isolated particles are considered as a one-molecule structure). The second sweep, performed over all distinct stacks, is necessary for merging particle lists belonging to the same column:

- (4) A stack k is chosen; all i molecules belonging to it are considered;
- (5) A second stack $l \neq k$ is selected and again, all j molecules belonging to it are considered;
- (6) All distinct pairs i, j are examined: if there is a pair such that $r_{ij} < r_t$ the two stacks belong to the same structure and are labeled with the same column index;
- (7) Points (4)–(6) are repeated in order to consider all distinct stacks found during the first sweep.

We have found this two-sweeps algorithm able to correctly identify samplewide structures without need of corrections for avoiding artifacts due to the periodic boundaries.

APPENDIX B: HELICAL AGGREGATES ANALYSIS

Here, we discuss the algorithm used for the computation of the average $P(r_{ij}, \alpha_{ij})$ histogram. If an aggregate possesses a rototranslational axis this will be coincident with the mean axis of the column. So, the first part of the algorithm is involved in finding for each column the axis $\hat{\mathbf{n}}_c$ (with orientation θ_n and φ_n) passing through the centroid of the aggregate. The optimal orientation of the vector $\hat{\mathbf{n}}_c$ is determined with the following fitting procedure:

- (1) A columnar aggregate is sampled from the current configuration with the procedure of Appendix A. The aggregate is formed by N_c particles with positions \mathbf{r}_i , with respect to the laboratory frame. The initial condition $\hat{\mathbf{n}}_c \parallel \hat{\mathbf{Z}}$, i.e., $\theta_n = 0$, and $\varphi_n = 0$ is assumed;
- (2) The centroid $\mathbf{r}_0 = (1/N_c) \sum_{i=1}^{N_c} \mathbf{r}_i$ of the aggregate is determined and all positions $\mathbf{p}_i = \mathbf{r}_i - \mathbf{r}_0$ are then referred to it ($\hat{\mathbf{n}}_c$ is assumed to go through \mathbf{r}_0);
- (3) The projections $\mathbf{s}_i = (\mathbf{p}_i \cdot \hat{\mathbf{n}}_c) \hat{\mathbf{n}}_c$ along the axis $\hat{\mathbf{n}}_c$ and all distance vectors $\mathbf{d}_i = \mathbf{p}_i - \mathbf{s}_i = d_i \hat{\mathbf{d}}_i$ from the column axis are calculated as well. These quantities are in turn used to compute the sum $D = \sum_{i=1}^{N_c} \mathbf{d}_i \cdot \mathbf{d}_i$ of squared distances from the axis;
- (4) Minimization of function D in terms of θ_n and φ_n , i.e., step (3) is repeated until the optimal axis $\hat{\mathbf{n}}_c$ is found.

The second step of the algorithm deals with the actual computation of the two-dimensional histogram $P(r_{ij}, \alpha_{ij})$. Notice that we define the histogram as a function of r_{ij} instead of its projection d_n along the column axis $\hat{\mathbf{n}}_c$ because in the columnar phase the two choices give similar results while in the isotropic phase the latter distance would not be defined and d_n would consequently assume random values (see Fig. 18). This calculation involves:

- (5) Computation of the scalar product $s_{ij} = \hat{\mathbf{d}}_i \cdot \hat{\mathbf{d}}_j = \cos(\alpha_{ij})$ and triple product $v_{ij} = \mathbf{d}_i \times \mathbf{d}_j \cdot \mathbf{r}_{ij}$;
- (6) Computation of $\alpha_{ij} = \arccos(s_{ij})$ if $v_{ij} > 0$, otherwise, if $v_{ij} < 0$ define $\alpha_{ij} = 2\pi - \arccos(s_{ij})$;
- (7) Update of $P(r_{ij}, \alpha_{ij})$ by increasing by one the histogram bin corresponding to the current values of r_{ij} and α_{ij} ;
- (8) Steps (8)–(9) are repeated for all distinct pairs i, j in the aggregate;
- (9) Steps (1)–(11) are repeated for all distinct aggregate structures of all MC configurations analyzed. Finally, the histogram $P(r_{ij}, \alpha_{ij})$ is normalized.

APPENDIX C: CHIRAL COLUMNS NOTATION

In this Appendix, we define the three-symbol coding we have used to identify model columnar structures depicted in Figs. 4 and 5. The first symbol h is used to specify the presence of a helical distribution of centres of mass. In addition, we use a bar, e.g., \bar{h} , to indicate the lack of a certain feature, in this case the absence of a helical structure. A subscript θ , (or $\bar{\theta}$) is then used to label the presence (or absence) of tilted $\hat{\mathbf{z}}_i$ molecular axes with respect to the column orientation $\hat{\mathbf{n}}_c$. A second subscript indicates the twist between neighboring

particles, which is a further molecular rotation φ around the \hat{z}_i molecular axis. Differently from θ , these φ rotations sum up along the column, so the first molecule is rotated by φ , the second by 2φ , the third by 3φ , and so on. When $\theta \neq 0$ (tilted column) the φ rotation can be performed before ($\varphi\theta$) or after ($\theta\varphi$) the tilt, a possibility that of course does not exist when $\theta=0$. The different non helical columnar structures we take into account can be described as follows:

($\bar{h}_{\theta\bar{\varphi}}$), columnar structure characterized by the absence of molecular tilt with respect to the column axis and the absence of twist between neighboring particles. So we have $\hat{r}_{ij} \cdot \hat{n}_c = 1$, $\hat{z}_i \cdot \hat{n}_c = 1$, and $\hat{z}_i \cdot \hat{z}_j = 1$, and also transversal axes are mutually parallel $\hat{x}_i \cdot \hat{x}_j = 1$.

($\bar{h}_{\theta\varphi}$), tilted columnar structure, $\hat{z}_i \cdot \hat{n}_c = \cos \theta$, while $\hat{r}_{ij} \cdot \hat{n}_c = 1$, and $\hat{z}_i \cdot \hat{z}_j = 1$, and $\hat{x}_i \cdot \hat{x}_j = 1$.

($\bar{h}_{\varphi\theta}$), twisted columnar structure where every molecular \hat{x}_i axis forms a nonzero φ angle with the neighboring \hat{x}_j axes, $\hat{r}_{ij} \cdot \hat{n}_c = 1$, and $\hat{z}_i \cdot \hat{n}_c = 1$, and $\hat{z}_i \cdot \hat{z}_j = 1$, and for neighboring i, j particles $\hat{x}_i \cdot \hat{x}_j = \cos \varphi$.

($\bar{h}_{\theta\varphi}$), tilted and twisted columnar structure with $\hat{r}_{ij} \cdot \hat{n}_c = 1$, and $\hat{z}_i \cdot \hat{n}_c = \cos \theta$, and $\hat{z}_i \cdot \hat{z}_j = 1$, and for neighboring i, j particles $\hat{x}_i \cdot \hat{x}_j = \cos \varphi$.

($\bar{h}_{\varphi\theta}$), twisted and tilted columnar structure with $\hat{r}_{ij} \cdot \hat{n}_c = 1$, and $\hat{z}_i \cdot \hat{n}_c = \cos \theta$, and $\hat{z}_i \cdot \hat{z}_j \neq 1$, and for neighboring i, j particles $\hat{x}_i \cdot \hat{x}_j \neq 1$.

We have shown in Fig. 4 some representative views of these chiral columns. In a similar way we have built the model structures of Fig. 5, namely, $h_{\theta\bar{\varphi}}$, $h_{\theta\varphi}$, $h_{\bar{\varphi}\theta}$, $h_{\varphi\theta}$, and $h_{\varphi\theta}$, where besides the same orientational distributions seen so far, the centres of mass also describe a helix with radius $0.1\sigma_0$ and pitch $3.6\sigma_0$.

¹J. W. Goodby, J. Mater. Chem. **1**, 307 (1991).

²A. H. Harris, R. D. Kamien, and T. C. Lubensky, Rev. Mod. Phys. **71**, 1745 (1999).

³H. Engelkamp, S. Middelbeek, and R. J. M. Nolte, Science **284**, 785 (1999).

⁴M. Albrecht, Chem. Rev. **101**, 3457 (2001).

⁵T. Nakano and Y. Okamoto, Chem. Rev. **101**, 4013 (2001).

⁶P. Cintas, Angew. Chem., Int. Ed. Engl. **41**, 1139 (2002).

⁷D. Coates and G. W. Gray, Mol. Cryst. Liq. Cryst. **24**, 163 (1973).

⁸D. Guillon, Struct. Bonding (Berlin) **95**, 41 (1999).

⁹G. Yan and T. C. Lubensky, J. Phys. II **7**, 1023 (1997).

¹⁰H. Bock and W. Helfrich, Liq. Cryst. **18**, 707 (1995).

¹¹D. Krücker, H.-S. Kitzerow, G. Heppke, and V. Vill, Ber. Bunsenges. Phys. Chem. **97**, 1371 (1993).

¹²T. Chuard, S. J. Cowling, M. Fernandez-Ciurleo, I. Jauslin, J. W. Goodby, and R. Deschenaux, Chem. Commun. (Cambridge) **21**, 2109 (2000).

¹³K. Praefcke, A. Eckert, and D. Blunk, Liq. Cryst. **22**, 113 (1997).

¹⁴J. Barberá, A. Elduque, R. Giménez, F. J. Lahoz, J. A. López, L. A. Oro, and J. L. Serrano, Inorg. Chem. **37**, 2960 (1998).

¹⁵J. Barberá, R. Iglesias, J. L. Serrano, T. Sierra, M. R. de la Fuente, B. Palacios, M. A. Pérez-Jubindo, and J. T. Vázquez, J. Am. Chem. Soc. **120**, 2908 (1998).

¹⁶T. Sierra and J. L. Serrano, Chem.-Eur. J. **6**, 759 (2000).

¹⁷J. G. Gay and B. J. Berne, J. Chem. Phys. **74**, 3316 (1981).

¹⁸M. P. Allen and D. J. Tildesley, *Computer Simulation of Liquids* (Clarendon, Oxford, 1987).

¹⁹D. Frenkel and B. Smit, *Understanding Molecular Simulation: From Algorithms to Applications* (Academic, San Diego, 1996).

²⁰*Advances in the Computer Simulations of Liquid Crystals*, edited by P. Pasini and C. Zannoni (Kluwer, Dordrecht, 2000).

²¹R. Berardi, C. Fava, and C. Zannoni, Chem. Phys. Lett. **236**, 462 (1995).

²²R. Berardi, C. Fava, and C. Zannoni, Chem. Phys. Lett. **297**, 8 (1998).

²³C. Zannoni, in *Physical Properties of Liquid Crystals*, edited by D. A. Dunmur, A. Fukuda and G. R. Luckhurst (EMIS, IEE, London, 2000), Vol. 1, Chap. 12.2.

²⁴C. Zannoni, J. Mater. Chem. **11**, 2637 (2001).

²⁵M. E. Rose, *Elementary Theory of Angular Momentum* (Wiley, New York, 1957).

²⁶H.-G. Kuball, Liq. Cryst. Today **9**, 1 (1999).

²⁷A. Ferrarini and P. L. Nordio, J. Chem. Soc., Perkin Trans. 2 **2**, 455 (1998).

²⁸L. Feltre, A. Ferrarini, F. Pacchiale, and P. L. Nordio, Mol. Cryst. Liq. Cryst. **290**, 109 (1996).

²⁹H. Sun, J. Phys. Chem. B **102**, 7338 (1998).

³⁰R. Berardi, S. Orlandi, and C. Zannoni, J. Chem. Soc., Faraday Trans. **93**, 1493 (1997).

³¹C. Zannoni, in *The Molecular Physics of Liquid Crystals*, edited by G. R. Luckhurst and G. W. Gray (Academic, London, 1979), Chap. 3.

³²F. Biscarini, C. Chiccoli, F. Semeria, P. Pasini, and C. Zannoni, Phys. Rev. Lett. **75**, 1803 (1995).

³³F. H. Stillinger, Science **267**, 1935 (1995).

³⁴L. Blum and A. J. Torruella, J. Chem. Phys. **56**, 303 (1972).

³⁵A. J. Stone, Mol. Phys. **36**, 241 (1978).

³⁶R. Berardi and C. Zannoni, J. Chem. Phys. **113**, 5971 (2000).

³⁷C. Zannoni and M. Guerra, Mol. Phys. **44**, 849 (1981).

³⁸S. L. Altmann, *Rotations, Quaternions, and Double Groups* (Clarendon, Oxford, 1986).

³⁹P. Dierckx, *Curve and Surface Fitting with Splines, Monographs on Numerical Analysis* (Oxford University Press, Oxford, 1993).